Title

Morphology of Shear-Induced Colloidal Aggregates in Porous Media: Consequences for Transport, Deposition, and Re-entrainment

Journal

Environmental Science and Technology, 54(9)

ISSN

0013-936X

Authors

Perez, Alejandro J
Patiño, Janis E
Soos, Miroslav
et al.

Publication Date

2020-05-05

DOI

10.1021/acs.est.9b05744

Peer reviewed

Environmental Science & Technology

pubs.acs.org/est

Article

Morphology of Shear-Induced Colloidal Aggregates in Porous Media: Consequences for Transport, Deposition, and Re-entrainment

Alejandro J. Perez, Janis E. Patiño, Miroslav Soos, and Verónica L. Morales*

Cite This: *Environ. Sci. Technol.* 2020, 54, 5813−5821

Read Online

ACCESS | Metrics & More | Article Recommendations | Supporting Information

ABSTRACT: Colloid deposition in granular media is relevant to numerous environmental problems. Classic filtration models assume a homogeneous pore space and largely ignore colloid aggregation. However, substantial evidence exists on the ubiquity of aggregation within porous media, suggesting that deposition is enhanced by it. This work studies the deposition process in relation to aggregate size and structure. We demonstrate that aggregation is induced at typical groundwater velocities by comparing the repulsive DLVO force between particle pairs to the hydrodynamic shear force opposing it. Column experiments imaged with high-resolution X-ray computed tomography are used to measure aggregate structure and describe their morphology probability distribution and spatial distribution. Aggregate volume and surface area are found to be power-law distributed, while Feret diameter is exponentially distributed with some flow rate dependencies caused by erosion and restructuring by the fluid shear. Furthermore, size and shape of aggregates are heterogeneous in depth, where a small number of large aggregates control the concentration versus depth profile shape. The range of aggregate fractal dimensions found (2.22−2.42) implies a high potential for restructuring or breaking during transport. Shear-induced aggregation is not currently considered in macroscopic models for particle filtration, yet is critical to consider in the processes that control deposition.

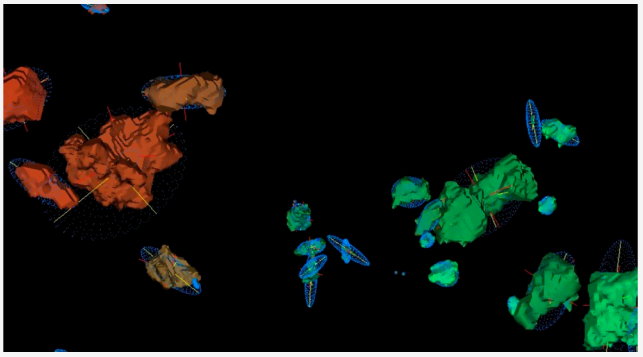

INTRODUCTION

Colloid phenomena play an important role in porous media processes, including environmental fate and transport of colloids, colloid-associated contaminants, and nanomaterials;[1−3] granular media filtration;[4] clogging;[5,6] and soil structure.[7] Numerous studies have suggested that aggregation can notably affect colloidal toxicity,[8−11] reactivity,[11−14] and environmental transport.[15−20] For transport, aggregate structure has been shown to have a strong impact on deposition and mobilization,[16−21] although the detailed processes are not well understood.

According to colloid filtration theory (CFT), particle deposition in porous media occurs in sequential steps for transport and attachment.[22] During transport, particles are brought to the vicinity of a collector by Brownian diffusion, interception, and gravitational sedimentation. During attachment, particles interact with the collector surface at very short distances thought to be driven in large part by Derjaguin−Landau−Verwey−Overbeek (DLVO) interactions.[23,24] The steady-state solution of CFT predicts that the depth dependence of particle accumulation should be exponential, which is frequently discrepant with experimental results. A key assumption made by CFT is that particles travel and interact with collector surfaces individually. However, direct evidence of the ubiquity of aggregation within porous media by numerous studies[15−17,19,20,25] suggests that this assumption is mechanistically incorrect, and that aggregation is responsible for enhanced deposition. To the authors' knowledge, Legg et al.[17] is the only study to present experimental evidence that particles preaggregate in the bulk fluid and subsequently deposit onto collectors as sparse-fractal aggregates (low-density), hinting that ripening is not the only mechanism through which aggregates deposit in the pores.

To correct for aggregation effects on the transport step, some studies propose to use an equivalent size given by the radius of gyration (or hydrodynamic size) of the aggregate and its effective density given by the fractal dimension, both of which impact the suspension's diffusivity,[18,26] drag,[18,27,28] and sedimentation.[29] Conversely, Lin and Wiesner[18] show that the size of the primary particle, not its aggregation state, determines the magnitude of the strength of colloidal

Received: September 25, 2019
Revised: January 21, 2020
Accepted: March 17, 2020
Published: March 17, 2020

interaction within the framework of DLVO theory; hence implying that the attachment step needs no correction. Moreover, very large aggregates are further immobilized by straining processes.[30,31] The dynamic process of deposition involves attachment, detachment, as well as local erosion and rearrangement of existing colloidal deposits. Various recent studies have sought to correlate colloid deposition in porous media with aggregate structure, paying close attention to aggregate fractal dimension.[17−21,32] Beyond aggregate compactness and size, however, morphologic properties like sphericity expose the ability of amorphous clusters to move across pore spaces given their orientation and response to shear flow.[27,33−37]

It is well-known that the size and structure of colloidal aggregates is affected by chemical conditions,[17] primary particle shape,[38] and most importantly by the fluid flow to which the suspension is exposed.[27,32] Hydrodynamic forces in the fluid experienced by suspended particles can enhance aggregation or deposition onto the porous medium surface. Similarly, shear stress on the aggregate can induce its breakup or restructuring.[17,18,20,27] In environmental hydrodynamic systems, aggregation is generally considered to be reaction limited, whereby a repulsive energy barrier must be overcome by chemical or mechanical means to obtain successful aggregation. Such reaction limited aggregation (RLA) tends to form more compact structures with characteristic fractal dimension of ∼2.1, compared to those formed by diffusion limited aggregation (DLA) with fractal dimension of ∼1.75.[18,39]

In porous media, the coupling between pore fluid flow, colloid deposit morphology, and pore geometry has been found to clog the pore space and affect the evolution of head-loss.[15,16,20,21] As deposition progresses, deposits on the filter media may locally alter the flow, which can impact subsequent removal of incoming particles or aggregates.[21] This consequently leads to a buildup of localized fluid shear that may restructure or break up aggregates, causing mobilization and redistribution of the colloidal material along the packed bed.[17] Results from simulations show that large particles and higher fluid velocities tend to form dense deposits of higher fractal dimension that are less prone to breakage and resuspension, while small particles and low fluid velocities produce more open deposits of lower fractal dimension.[21] Aggregates with lower fractal dimension have been shown to break more easily.[32] Frail aggregate deposits break in localized zones of high shear. This mobilizes colloidal material of lower fractal dimension, leaving behind a more compact deposit at the origin.[20] Redistribution of sloughed colloidal material locally recuperates the permeability of the pore space, permitting the colloidal filtration process to resume in a semiclean bed as a system with self-regulating negative feedback.[15]

In this study, direct measurements of the structure of colloid deposits in porous media are used to investigate the relationship between imposed flow rate, aggregate structure, and the mechanism for particle deposition. We consider the possibility that hydrodynamic shear can provide sufficient energy to overcome electrostatic repulsion between suspended colloids to induce aggregation and encourage deposition. Calculations of the opposing forces are presented to support our hypothesis. Detailed characterization of colloidal aggregates is used to determine how flow rate controls the variability in formed aggregate size and morphology. We then examine how aggregate structure is linked to its ability to penetrate the packed bed, and use this to explain the concentration profile shape with depth. Lastly, aggregate mechanical properties are analyzed in light of their tendency to become unstable and undergo detachment (re-entrainment) during a physical or chemical disturbance.

MATERIALS AND METHODS

Materials. Custom made hollow glass microspheres coated in a 118 nm thick layer of silver were used as the silver colloids for experimentation (Microsphere Technology, Limerick, IE). Silver particles were deliberately chosen because they facilitate imaging with X-rays as described below. According to the manufacturer, their mean diameter is 14 ± 4 μm and density is 1.0 g mL^{-1}. Suspensions of 0.02 g mL^{-1} were prepared in Milli-Q water (pH 7, and ionic strength of 0 mM unless otherwise indicated) and used in experiments within 10 h. Borosilicate glass beads of 1 mm mean diameter were used as the porous medium (Sigma-Aldrich). The glass beads were chemically pretreated by sequential soaking in concentrated HCl for 24 h to remove metal oxides, repeated rinsing with Milli-Q water until the pH was neutral, and then baked overnight at 550 °C to remove organic impurities.

Small Angle Light Scattering. Small angle light scattering (SALS) was used to monitor the silver aggregation extent prior to injection of the colloidal suspension into the columns for transport experiments. Here, the average radius of gyration of the clusters, $\langle R_g \rangle$, was measured under quiescent conditions (i.e., in the absence of hydrodynamic shear). The SALS instrument used in this work (Mastersizer 2000, Malvern, UK) has a working angle range θ = 0.02−40°, a wavelength of incident light λ_0 = 633 nm, and an intensity acquisition frequency of 1000 s^{-1}. Details of the SALS system can be found elsewhere,[40] and the calculations for estimating $\langle R_g \rangle$ are described in the Supporting Information (SI). SALS measurements demonstrate that the chosen water chemistry creates unfavorable conditions for aggregation in our suspension. Hence, a physical factor must be responsible for any observed aggregation during transport, where hydrodynamic shear is present.

Opposing DLVO Repulsive and Hydrodynamic Shear Forces. Colloidal particles are typically stabilized by forces of electrostatic origin, indicating that the repulsive force barrier must be overcome for charge-stabilized particles to aggregate. In a porous medium, a suspension is subjected to shear by the nature of the flow, which can be sufficiently strong to "push" repulsive particles together. Hence, the occurrence of shear-induced aggregation can be assumed to depend on the balance between DLVO and shear forces.[41] We determine the propensity for shear-induced aggregation by considering the maximum shear force available at a given shear rate in comparison to the repulsive force barrier of the suspension.

To compute the repulsive barrier (the maximum force), the force between interacting identical particles was determined from classical DLVO theory. Repulsive electric double-layer force, F_{edl}, was estimated from the derivative of the potential energy of interaction as approximated by Gregory[42] as

$$F_{edl} = \frac{64\pi a \eta_\infty k_B T}{\kappa} \gamma^2 \exp(-\kappa h) \quad (1)$$

where a is the radius of the colloid, η_∞ is the bulk number density of ions, k_B is the Stefan−Boltzmann constant, T is the absolute temperature, $\gamma = \tanh(ze\zeta/4k_BT)$ is the reduced

https://dx.doi.org/10.1021/acs.est.9b05744
Environ. Sci. Technol. 2020, 54, 5813−5821

surface potential of the colloid as a function of the ion valence, z, electron charge e, and the measured colloid zeta potential, ζ (measured with ionic strength of 1 mM KCl), κ is the inverse Debye length, and h is the separation distance. Attractive van der Waals force, F_{vdW}, was estimated from the derivative of the retarded potential energy of interaction proposed by Gregory[43] as

$$F_{vdW} = -\frac{Aa\left(1 + \frac{28}{\lambda}h\right)}{12\left(h + \frac{14}{\lambda}h^2\right)^2} \quad (2)$$

where A is the system's Hamaker constant and λ is the characteristic wavelength of the interaction, which has a value of l00 nm for most materials.[44] The total force profile, F, is the sum of F_{vdW} and F_{edl}.

Nanoroughness on the surface of the colloidal particles were qualitatively observed with scanning electron microscopy (see Figure S2) and accounted for in the total force profile as per the work of Tokzaban and Bradford.[45] Surface roughness effects were incorporated into DLVO calculations to quantify the magnitude of the total force of nonsmooth colloids. A simplified random representation of random roughness is considered with pillars of height h_r in the range of 35−50 nm and surface density f between 0.5−4%. The mean total interaction energy, $F_m(h)$, is estimated as the linear combination of interaction energies of asperity element tops and the smooth surface bottom as

$$F_m(h) = (1 - f)F(h + h_r) + (f)F(h) \quad (3)$$

To determine the maximum shear force available, the maximum hydrodynamic force, $F_s^{(max)}$, for two equal-sized spheres approaching each other in a simple shear flow was calculated as per the work of Husband and Adams[46]

$$F_s^{(max)} = 3.06\pi\mu\langle R_g\rangle^2 G \quad (4)$$

where μ is the dynamic (shear) viscosity of the fluid and G is the measured shear rate in the column determined by eq S4. The force balance results are interpreted in consideration of the relevant interparticle and hydrodynamic forces involved.

Column Experiments. Cylindrical polypropylene columns (4.7 mm inner diameter and 35 mm length) were wet-packed to a depth of approximately 30 mm with the clean glass beads and maintained fully water saturated. A piece of stainless steel mesh was placed at the top and bottom of the packed bed to keep the glass beads in the column and out of the influent/effluent tubing. The packed columns were conditioned with five pore volumes of Milli-Q water prior to transport experiments in a downward flow arrangement. Then, 400 μL of the colloidal suspension was injected at a continuous flow rate, followed by flushing with particle-free background solution of Milli-Q water until the effluent concentration returned to baseline levels. Effluent concentration was measured in a flowthrough cuvette by UV−vis spectrophotometry at a wavelength of 850 nm in 30 s intervals. The flow rate was controlled by a push−pull syringe pump that exactly matched the rate at which influent was dispensed at the top, and effluent withdrawn from the bottom of the column. Triplicate experiments were conducted for two different flow rates, 3.2 and 6.4 mL h^{-1}. Following each experiment, the column was sealed at both ends to prevent evaporation, maintained in a vertical position, and immediately analyzed with tomographic imaging on site to ensure relocation did not change particle deposition patterns.

XCT Scanning and Image Processing. X-ray computed tomography (XCT) imaging of the column was conducted with a benchtop scanner (ZEISS Xradia, MicroXCT-200) at the University of California, Davis, to obtain a detailed three-dimensional static picture of the distribution of colloid deposits in the porous medium. The materials that make up the packed column and the colloidal suspension were selected to obtain the greatest contrast and best quality images with XCT. To achieve a voxel resolution of 10 μm, the sample was scanned in multiple segments that were subsequently stitched together during reconstruction. The power of the X-ray source tube was set to 8 W with an energy of 40 kV. An Xradia LE#3 source filter was used to harden the spectrum and reduce beam-hardening artifacts. A complete 360° scan consisted of 1600 projections and required about 4 h per segment. Each scan produced projection data of the packed porous media in segments of length of ∼10 mm. The projection data of each segment was used to reconstruct a stitched image of the column. Reconstruction and stitching was done with XRADIA proprietary software, TXM Controller, TXM Reconstructor, and TXM Viewer.

Segmentation. Segmentation of the column images was performed with dedicated commercial software for XCT image analysis (Volume Graphics Studio Max and Amira). First, the images were preprocessed using a nonlocal mean filter to increase the signal-to-noise ratio. A hybrid segmentation approach, combining global thresholding and locally adaptive thresholding, was used to define regions of interest corresponding to the colloid deposits and the pore space. Next, global histogram thresholding was used to remove voxels corresponding to the silver colloids, as the sample material with highest X-ray attenuation and largest histogram gray values. Then, locally adaptive thresholding was used to perform precise segmentation of the pore space with operator-specified input parameters of the existing solid and liquid phases. Region grower was used to refine particularly noisy pore space segmentation results. Segmented images of colloid deposits and the pore space were finally used for aggregate morphology and shear rate distribution analyses, respectively.

Aggregate Morphology. Image processing and analysis of the morphological characteristics of colloidal deposits formed in porous media were performed using the software Fiji/ImageJ,[47] including the Particle Analyzer plugin in BoneJ[48] and Matlab. Particle Analyzer (with a mesh resampling factor of 1) identifies individual particle clusters and analyses their characteristics separately for volume (V); surface area (SA); Feret diameter (Fe), as maximum diameter; geometric centroid coordinates (x, y, z); and major (r_{Maj}), intermediate (r_{Int}), and minor (r_{Min}) radii of the best fit ellipsoid. Geometric sphericity $\left(\psi = \frac{(36\pi V^2)^{(1/3)}}{SA}\right)$ and aspect ratio $\left(AR = \frac{r_{Min}}{r_{Maj}}\right)$ were additionally determined from the plugin outputs. Aggregate cohesive force and compaction were determined from fractal dimension, D_3, obtained from the scaling of the number of primary particles in an aggregate, N, versus the ratio between the minimum radius of the aggregate, r_{Min}, and the primary particle radius, r_0, such that $N \sim (r_{Min}/r_0)^{D_3}$. N is approximated as the ratio of measured aggregate volume to primary particle volume. Our analysis considers six structural characteristics, M_i, measured for each aggregate: V, SA, Fe, ψ, AR, and D_3. The

https://dx.doi.org/10.1021/acs.est.9b05744
Environ. Sci. Technol. 2020, 54, 5813−5821

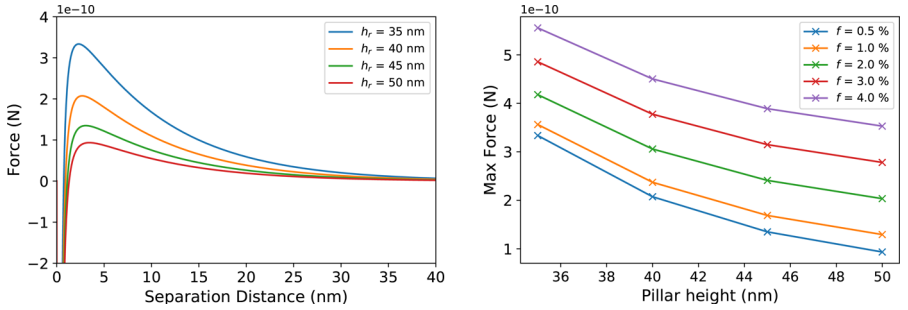

Figure 1. (Left) DLVO force profiles as a function of particle separation, corrected for nanoroughness of density$f$ = 0.5%, and variable pillar height, h_r. (Right) Force barrier for various combinations of roughness density and pillar height.

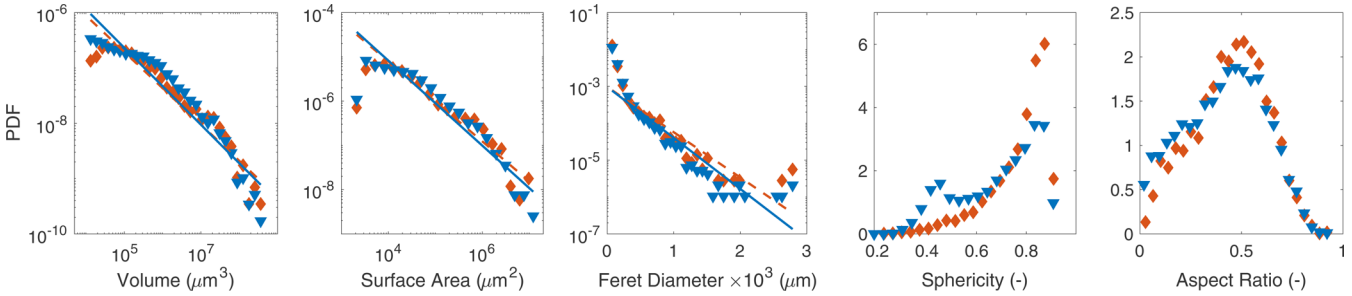

Figure 2. Probability density functions of colloidal aggregate size and morphology characteristics. Symbols correspond to experiments of slow (diamonds) and fast (triangles) flow rates. Lines indicate the power law or exponential fit to distributions for volume, surface area, and Feret diameter for slow (dashed) and fast (solid) flow rates.

SI describes various control tests performed on the data to determine its quality and the smallest cluster size distinguishable from noise, given that individual primary particles cannot be resolved with this experimental setup.

Statistical Analysis. Global probability density functions were assessed for the first five aggregate morphologies to evaluate their distribution and relative abundance as $p(M_i)$. Cross-correlations were used to measure similarities between morphologic characteristics. Significant correlations were those with an absolute Pearson's linear coefficient greater than 0.7 and a p-value below 0.05. Conditional probabilities were used to evaluate different shape characteristics relative to aggregate volume as $p(M_i > M_i'|V)$. Trends in depth were evaluated with joint probability density function for each morphological characteristic as $p(M_i, z)$. All statistical analysis was restricted to clusters containing at least 10 primary particles. Fractal dimension was evaluated for clusters of at least 30 primary particles as recommended by Lee and Kramer[49] to reduce uncertainty in the estimation of N due to partial volume effects, which diminishes with increasing aggregate size.

RESULTS AND DISCUSSION

Suspension Stability. Average radius of gyration of the colloid suspension prior to column injection was measured with SALS as 26.18 μm. This suggests that the suspension is stable under quiescent conditions (absence of fluid shear), and that formed colloid clusters are on average triplets over the course of a 20 min time period. This measurement is used as a control to compare the aggregate size distributions achieved when the suspension is subjected to fluid shear during transport through porous media, as discussed below.

Opposing DLVO Repulsive and Hydrodynamic Shear Forces. A comparison between opposing DLVO repulsive and hydrodynamic shear forces enables determination of the critical hydrodynamic force required to onset shear-induced aggregation. The following presents a force balance approach similar to that used by Husband and Adams[46] who studied the forces involved in orthokinetic aggregation. Figure 1 shows exemplary DLVO force profiles of interacting colloids, considering nanoscale surface roughness (profiles corresponding to other densities are not shown). From these data, we estimate that the force barrier magnitude F_m could have a range of 9.3 × 10^{-11} to 4.9 × 10^{-10} N. The maximum hydrodynamic force (from eq 4) was determined to have a magnitude of $F_s^{(max)}$ = 2.8 × 10^{-10} and 5.6 × 10^{-10} N for the slow and fast flow rates, respectively. Hence, the hydrodynamic shear over the quiescent triplets is confirmed to be large enough to overcome the repulsive force stabilizing the suspension and stimulate efficient aggregation, particularly for surface roughness of characteristically large pillar heights or low densities. The maximum shear force is found in 16% and 19% (8 and 10 times per mm^3 of media) of the channels in the column for slow and fast flow rates, respectively (also illustrated in Figures S4 and S5). An example of the lower force requirement occurrence for a specific suspension is given in section S3. The authors note that lubrication forces are not accounted for since the surface roughness in the system is rather large. As noted by Husband and Adams,[46] considering the relevant hydrodynamic and interparticle forces involved at constant water chemistry, too low a shear rate applied to a suspension will only break weak floccs formed at the secondary minimum. An increase in shear will result in productive aggregation into the primary minimum. Increasing the shear rate further may destroy previously formed aggregates.

Aggregate Size and Morphology. Global probability distribution functions for each characteristic measured are shown in Figure 2 for the two flow rates tested. The range of values for all morphologies is similar for both flow rates.

https://dx.doi.org/10.1021/acs.est.9b05744
Environ. Sci. Technol. 2020, 54, 5813−5821

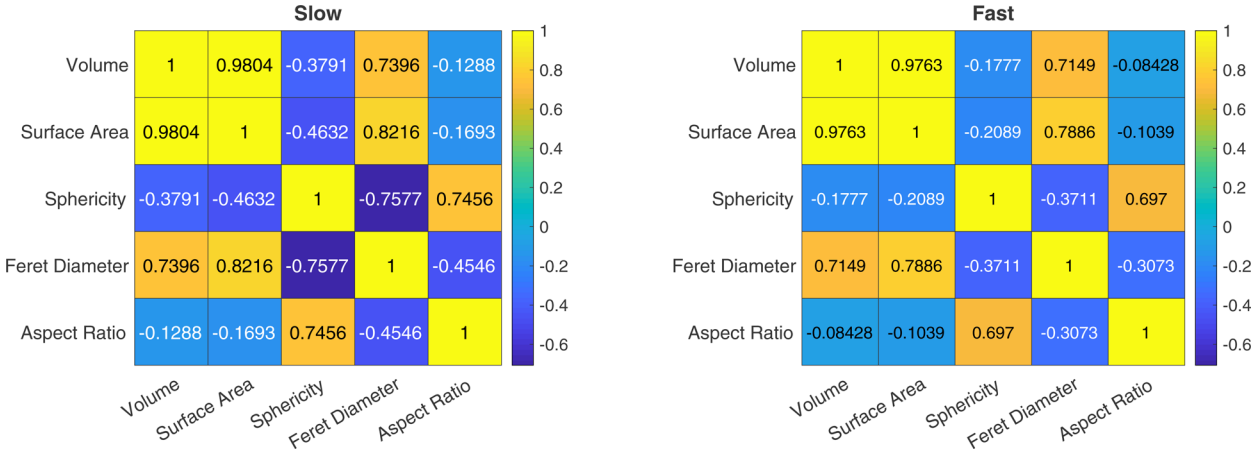

Figure 3. Pearson's rank correlation matrix of aggregate morphological characteristics for experiments conducted at slow and fast flow rates.

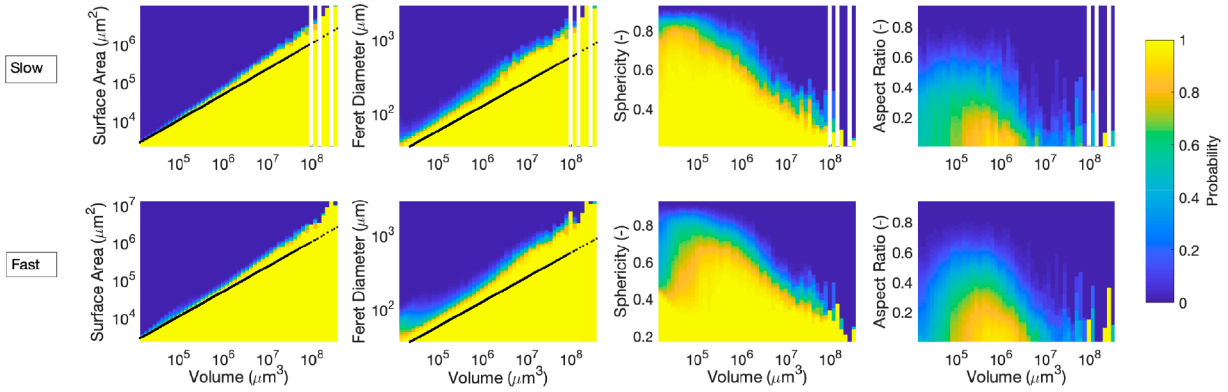

Figure 4. Relationship between volume and different morphological characteristics for corresponding aggregates in a given population. Top (bottom) panels correspond to experiments run at slow (fast) flow rates. The coloring gives the probability $p(M_i > M_i'|V)$ that an aggregate of morphology, M_i, of given volume, V, takes a value larger than M_i', where M_i' is plotted along the vertical axis. Reference lines for surface area and Feret diameter of ideal spheres of the same given volume are shown in black. The blank spaces at high values of V indicate the absence of aggregates of such size.

Volume and surface area are power law distributed ($p(M_i) = mM_i^B$, where m is a constant and B is the scaling exponent), while Feret diameter shows an exponential distribution ($p(M_i) = me^{BM_i}$, where m is a constant and B is the power exponent). These distributions capture the strong heterogeneity of the colloidal aggregates. The fitted scaling exponents, B, increase with flow rate as shown in Table S1. The distributions for volume and surface area are power-law and, therefore, are also scale invariant. Their fitted scaling exponents, $B < 1$, indicate that they also lack a well-defined mean and variance, since a power-law x^{-B} has a well-defined mean over $x \in [1, \infty)$ only if $B > 2$, and a finite variance only if $B > 3$. This shows that although very few voluminous aggregates contribute to most of the deposited colloidal mass, this small number of aggregates can strongly influence the concentration distribution in depth. Feret diameter, on the other hand, has well-defined moments with lower variability between diameters for the most and least probable aggregates. The distribution of sphericity is flow rate-dependent. Fast flow rates display a bimodal distribution with peaks at 0.4 and 0.8, where the more spherical second mode is more probable. Slow flow rates have an unimodal distribution skewed to higher values that peaks at 0.8. The distribution of aspect ratio approaches a Gaussian and peaks similarly at 0.4 for both flow rates. The mean and variance of the aspect ratio and sphericity distributions are reported in Table S1. The bimodal quality of sphericity may be attributed to aggregate stretching due to the increased shearing at higher flow rates, which is in agreement with increased skewness in the distribution for aspect ratio at the same flow conditions.

A major factor affecting an aggregate's response to flow is its shape.[27] On the one hand, the volume of an aggregate informs on its tendency to be strained and immobilized during transport through porous media.[31,36] On the other hand, Feret diameter, sphericity, and aspect ratio inform about its susceptibility to pass through a pore throat based on its orientation with the flow. Spherical aggregates rotate smoothly in the presence of velocity gradients, while elongated aggregates experience oscillations of angular velocity in shear flows.[27] To the authors' knowledge, the effects of aggregate elongation morphology on deposition and transport kinetics in porous media have not been studied. However, the effect of primary particle aspect ratio on straining and transport has received some attention, albeit with conflicting results.[33−37] A greater amount of straining has been shown to occur for elongated primary particles, compared to spherical ones.[34,35] However, observations of the opposite have also been reported,[33,36] attributing the effect to preferred rotation and orientation of the particle as it approaches a pore constriction.

https://dx.doi.org/10.1021/acs.est.9b05744
Environ. Sci. Technol. 2020, 54, 5813−5821

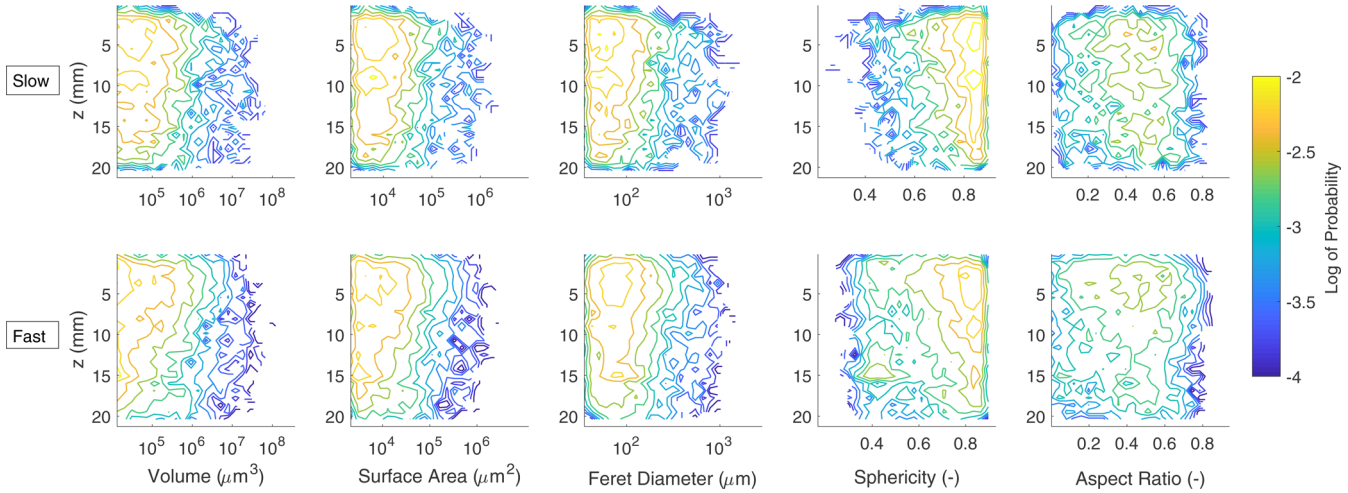

Figure 5. Spatial distribution of aggregate morphology characteristics with depth. Top (bottom) panels correspond to experiments run at slow (fast) flow rates. Colored contours give the probability $p(M_i, z)$ that an aggregate of morphology, M_i, is found at depth, z.

That is, the minor axis of the particle is considered to be the critical dimension controlling straining retention processes.

In addition to the insights gained from individual aggregate structure distributions, it is useful to know how structural characteristic pairs are correlated. Figure 3 shows correlation matrices of the five characteristics investigated. *P*-values for all pairs were less than 0.05, signifying statistical significance across the board. Positive correlations with Pearson coefficients greater that 0.7 were found between volume-to-surface area, volume-to-Feret diameter, and Feret diameter-to-surface area for both flow rates. These three characteristics are strongly correlated in large part because of the prevalence of small aggregates with maximal surface area and limited configuration for Feret diameter. Anticorrelations were found only between Feret diameter-to-sphericity at slow flow rates. This could be attributed to the elongated shape of larger nonspherical aggregates. In general, correlations between pairs were weaker for fast compared to slow flow rates, corroborating the increased heterogeneity with higher shear.

The distribution of the different measured morphologic characteristics relative to the given aggregate volume are shown in the conditional probability plots, $p(M_i > M_i'|V)$, of Figure 4. Reference lines for surface area and Feret diameter of ideal spheres of the same given volume are shown in black. Trends across the two flow rates are similar for all characteristics in aggregates larger than 10^{-5} μm^3. Generally, the surface area and Feret diameter of aggregates increasingly depart from that of a perfect sphere as volume increases, suggesting that small aggregates approach spheres but acquire an elongated geometry as they grow in size.[50] A decrease in sphericity and aspect ratio with increasing volume for aggregates larger than 10^{-5} μm^3 corroborates this trend. Differences in flow rate are seen, however, in Feret diameter and sphericity for aggregates smaller than 10^{-5} μm^3. Small aggregates formed with fast flow rates have a broader range of Feret diameters and depart more strongly from the ideal sphere reference line than their slow flow rate counterparts. Similarly, sphericity changes non-monotonically with volume for fast flow rates, while slow flow rate shows a fairly uniform distribution for this volume range. We speculate that large aggregates are retained by straining processes and become elongated by the hydrodynamic shear, which is stronger for higher flow rates in general, as well as locally where the pore is clogged by deposits of large aggregates.

Aggregate Distribution in Depth. Figure 5 presents the joint probability distribution of each aggregate characteristic with depth, $p(M_i, z)$. The probability of finding aggregates of a given size or structural characteristic in depth is shown by the colored equiprobable contours. The contours indicate a higher probability of finding aggregates of large volume, surface area, and Feret diameter near the surface (top) of the column, than at greater depths. This trend is evident in the cone-shaped contours. No dependence on flow rate was observed. Conceivably, larger aggregates become strained in the pore space and travel fewer pore lengths, relative to the longer distance traveled by smaller aggregates. We compare $p(V, z)$ (Figure 5 first column) with traditional deposition concentration profiles in depth, $S_{Ag} \propto \exp\left(\frac{-kz}{v}\right)$ (see Figure S8), which are independent of all aggregate characteristics. Here, S_{Ag} is the concentration of deposited silver, k is the first-order deposition kinetics term, z is depth, and v is the advective term. A stationary exponential profile is predicted by CFT, although hyperexponential profiles have been broadly reported in excavation experiments (e.g., Bradford et al.[51] and references therein). Given the small dimensions of our column, it is not possible to determine if our observed profiles are exponential or hyperexponential. In either case, $p(V, z)$ sheds light on why the concentration profiles have a (hyper)exponential shape, which is due to the small number of extremely large agglomerates found at shallow depths.

Fast flow rate conditions produce aggregates that approach a spherical shape near the top of the column and become elongated with depth (evident in the cone-shaped contours). In contrast, slow flow rate conditions produce aggregates that are dominantly spherical and show no depth dependency (evident in the vertical contours). These trends in depth are shared for aspect ratio between the two flow rates. Aggregate elongation is likely a result of exposure to higher shear from a faster flow rate. High shear could push aggregates deeper in the packed bed, elongate them with each passed pore throat, and selectively break mechanically weak and porous portions of the aggregate into smaller units that can travel deeper in the column but are not eluted from it. It cannot be ruled out that

https://dx.doi.org/10.1021/acs.est.9b05744
Environ. Sci. Technol. 2020, 54, 5813−5821

local detachment of entire deposits could occur at some locations within the porous medium.

Determination of Aggregate Mechanical Strength. Fractal dimension is here used as a metric to quantify an aggregate's mechanical strength and to understand its potential for restructuring by fluid shear. The fractal dimension of the entire aggregate population was smaller for slow, D_3 = 2.22 (2.20, 2.24), than for fast flow rates, D_3 = 2.42 (2.39, 2.44), where values in parentheses indicate the 95% confidence bounds (see Figure S9). Measurements of fractal dimension of subpopulations at multiple depth increments showed that D_3 did not change significantly with distance traveled by the aggregate (data not shown). It cannot be ruled out that the column might be insufficiently long to reveal the evolution of fractal dimension as a function of depth. The observed fractal dimensions in our aggregates confirms that the aggregation regime was RLA. Recall from the introduction that RLA has a characteristic fractal dimension of ∼2.1[18,39], with an upper bound close to 2.5 for aggregates that have undergone breakage.[39] For the lower observed D_3, aggregates have a higher potential for restructuring and breaking during porous media transport by the fluid shear to which the deposits are subjected, consistent with prior work.[32,39]

According to the calculations shown in the SI, the shear stress ranges can be coarsely approximated at $[1 \times 10^{-3}, 2 \times 10^{-2}]$ and $[2 \times 10^{-3}, 5 \times 10^{-2}]$ Pa for slow and fast flow rates, respectively. In agreement with conventional wisdom, aggregates exposed to higher shear stress at constant water chemistry are expected to have higher D_3 and vice versa. This is thought to result from increased breakage and restructuring of low D_3 aggregates into higher D_3 aggregates by the added stress. Previous studies have reported an increase in fractal dimension with flow velocity,[20,21,52] albeit for a range of velocities that are one or two orders of magnitude greater than the ones used here, which are typical for groundwater. Recognizing that larger aggregates deposit near the surface of a packed bed, it is conceivable that when these deposits have low fractal dimension they could be easily broken by physical or chemical perturbations. This could remobilize aggregates as smaller fragments and promote their transport to greater depths in the porous medium.

Environmental Implications. Colloids often exist in the subsurface as primary minimum aggregates that are formed by the imbalance of stabilizing colloidal forces and the hydrodynamic shear of the flowing water that carries them. Aggregation may significantly reduce particle transport by increasing their hydrodynamic size. However, this study shows for the first time that the resulting aggregate size is power-law distributed and that the spatial distribution of the very large clusters dictates the concentration depth profile. From a modeling perspective, the broad distribution of particle (aggregate) sizes and compaction will affect the transport (single collector) coefficient but not its attachment coefficient, as outlined in CFT. This implies that colloids undergoing aggregation during transport in porous media move toward collectors by different proportions of CFT-considered transport mechanisms (diffusion, interception, sedimentation). As aggregates grow, they become less diffusive, while as aggregates break and restructure, their density changes affect their sedimentation potential. Experimental results showed that preferential formation of very large deposits of low fractal dimension occurs near the column inlet in steady state conditions. At greater penetration depths and higher shear, aggregates showed evidence for mild breakup and structural evolution. This implies that sporadic release and redistribution of particles during a physical or chemical disturbance is likely to disproportionately affect the small number of very large and frail aggregates near the inlet. Aggregate formation and breakage during realistic transient conditions should eventually produce clusters of stable size and level of compactness. Nevertheless, more detailed characterization of aggregate properties and their location during disturbance events is needed to predict when and where deposits form and become unstable.

■ ASSOCIATED CONTENT

Supporting Information

The Supporting Information is available free of charge at https://pubs.acs.org/doi/10.1021/acs.est.9b05744.

Small angle light scattering, SEM images of colloidal particles, estimates for shear rate and stress, XCT image analysis quality controls, PDF parameters of aggregate morphology characteristics, depth profiles in concentration, fractal dimension, and raw data (PDF)

■ AUTHOR INFORMATION

Corresponding Author

Verónica L. Morales − *Department of Civil and Environmental Engineering, University of California, Davis, California 95616, United States;* orcid.org/0000-0002-9595-6026; Phone: +1 (530)752-4008; Email: vermorales@ucdavis.edu

Authors

Alejandro J. Perez − *Department of Civil and Environmental Engineering, University of California, Davis, California 95616, United States;* orcid.org/0000-0002-8289-6722

Janis E. Patiño − *Department of Civil and Environmental Engineering, University of California, Davis, California 95616, United States*

Miroslav Soos − *Department of Chemical Engineering, University of Chemistry and Technology, Prague 166 28, Czech Republic;* orcid.org/0000-0002-9742-7160

Complete contact information is available at: https://pubs.acs.org/10.1021/acs.est.9b05744

Notes

The authors declare no competing financial interest.

■ ACKNOWLEDGMENTS

This work was supported in part by Marie Curie Actions (FP7-PEOPLE-2012-SoilArchnAg), the Social Science Research Council (Sloan Scholars Mentoring Network Grant), and the Hellman Fellowship. The authors thank Dr. Hua Wu for SALS measurements and assistance in data interpretation, and the anonymous reviewers for their constructive feedback.

■ REFERENCES

(1) de Jonge, L. W.; Kjaergaard, C.; Moldrup, P. Colloids and Colloid-Facilitated Transport of Contaminants in Soils: An Introduction. *Vadose Zone J.* **2004**, *3*, 321−325.

(2) Maynard, A. D.; Aitken, R. J.; Butz, T.; Colvin, V.; Donaldson, K.; Oberdorster, G.; Philbert, M. A.; Ryan, J.; Seaton, A.; Stone, V.; Tinkle, S. S.; Tran, L.; Walker, N. J.; Warheit, D. B. Safe handling of nanotechnology. *Nature* **2006**, *444*, 267−269.

(3) Ryan, J. N.; Elimelech, M. Colloid Mobilization and Transport in Groundwater. *Colloids Surf., A* **1996**, *107*, 1−56.

(4) Tien, C.; Payatakes, A. C. Advances in Deep Bed Filtration. *AIChE J.* **1979**, *25*, 737−759.
(5) Mays, D. C.; Hunt, J. R. Hydrodynamic and Chemical Factors in Clogging by Montmorillonite in Porous Media. *Environ. Sci. Technol.* **2007**, *41*, 5666−5671.
(6) Torkzaban, S.; Bradford, S.; Vanderzalm, J.; Patterson, B.; Harris, B.; Prommer, H. Colloid release and clogging in porous media: Effects of solution ionic strength and flow velocity. *J. Contam. Hydrol.* **2015**, *181*, 161−171.
(7) Dexter, A. Advances in Characterization of Soil Structure. *Soil Tillage Res.* **1988**, *11*, 199−238.
(8) Cheng, Y.; Yin, L.; Lin, S.; Wiesner, M.; Bernhardt, E.; Liu, J. Toxicity reduction of polymer-stabilized silver nanoparticles by sunlight. *J. Phys. Chem. C* **2011**, *115*, 4425−4432.
(9) Jiang, J.; Oberdoerster, G.; Biswas, P. Characterization of size, surface charge, and agglomeration state of nanoparticle dispersions for toxicological studies. *J. Nanopart. Res.* **2009**, *11*, 77−89.
(10) Jassby, D.; Farner Budarz, J.; Wiesner, M. Impact of aggregate size and structure on the photocatalytic properties of TiO2 and ZnO nanoparticles. *Environ. Sci. Technol.* **2012**, *46*, 6934−6941.
(11) Levard, C.; Hotze, E. M.; Lowry, G. V.; Brown, G. E. Environmental transformations of silver nanoparticles: impact on stability and toxicity. *Environ. Sci. Technol.* **2012**, *46*, 6900−6914.
(12) Tiede, K.; Hassellov, M.; Breitbarth, E.; Chaudhry, Q.; Boxall, A. Considerations for environmental fate and ecotoxiclogy testing to support environmental risk assessments for engineered nanoparticles. *J. Chromatogr.* **2009**, *1216*, 503−509.
(13) Li, X.; Lenhart, J. J. Aggregation and dissolution of silver nanoparticles in natural surface water. *Environ. Sci. Technol.* **2012**, *46*, 5378−5386.
(14) Hotze, E. M.; Bottero, J.-Y.; Wiesner, M. R. Theoretical framework for nanoparticle reactivity as a function of aggregation state. *Langmuir* **2010**, *26*, 11170−11175.
(15) Chen, C.; Gaillard, B.; Packman, A.; et al. Temporal evolution of pore geometry, fluid flow, and solute transport resulting from colloid deposition. *Water Resour. Res.* **2009**, *45*, W06416.
(16) Gaillard, J.-F.; Chen, C.; Stonedahl, S. H.; Lau, B. L. T.; Keane, D. T.; Packman, A. I. Imaging of colloidal deposits in granular porous media by X-ray difference micro-tomography. *Geophys. Res. Lett.* **2007**, *34*, L18404.
(17) Legg, B.; Zhu, M.; Comolli, L.; Gilbert, B.; Banfield, J. Impacts of ionic strength on three-dimensional nanoparticle aggregate structure and consequences for environmental transport and deposition. *Environ. Sci. Technol.* **2014**, *48*, 13703−13710.
(18) Lin, S.; Wiesner, M. Deposition of Aggregated Nanoparticles−A Theoretical and Experimental Study on the Effect of Aggregation State on the Affinity between Nanoparticles and a Collector Surface. *Environ. Sci. Technol.* **2012**, *46*, 13270−13277.
(19) Mays, D. C.; Cannon, O. T.; Kanold, A. W.; Harris, K. J.; Lei, T. C.; Gilbert, B. Static light scattering resolves colloid structure in index-matched porous media. *J. Colloid Interface Sci.* **2011**, *363*, 418−24.
(20) Roth, E.; Gilbert, B.; Mays, D. Colloid deposit morphology and clogging in porous media: Fundamental insights through investigation of deposit fractal dimension. *Environ. Sci. Technol.* **2015**, *49*, 12263−12270.
(21) Wiesner, M. Morphology of particle deposits. *J. Environ. Eng.* **1999**, *125*, 1124−1132.
(22) Yao, K.-M.; Habibian, M. T.; O'Melia, C. R. Water and Waste Water Filtration: Concepts and Applications. *Environ. Sci. Technol.* **1971**, *5*, 1105−1112.
(23) Derjaguin, B. V.; Landau, L. D. Theory of the Stability of Strongly Charged Lyophobic Sols and of the Adhesion of Strongly Charged Particles in Solutions of Electrolytes. *Acta Physicochim. URSS* **1941**, *14*, 733−762.
(24) Verwey, E. J. W.; Overbeek, J. T. G. *Theory of the Stability of Lyophobic Colloids: The Interaction of Sol Particles Having an Electric Double Layer*; Elsevier Publishing Company, 1948.
(25) Zhang, W.; Morales, V.; Cakmak, M.; Salvucci, A.; Geohring, L.; Hay, A.; Parlange, J.; Steenhuis, T. Colloid transport and retention in unsaturated porous media: effect of colloid input concentration. *Environ. Sci. Technol.* **2010**, *44*, 4965−4972.
(26) Chen, K. L.; Elimelech, M. Aggregation and deposition kinetics of fullerene (C60) nanoparticles. *Langmuir* **2006**, *22*, 10994−11001.
(27) Fellay, L. S.; Twist, C.; Vanni, M. Motion of rigid aggregates under different flow conditions. *Acta Mech* **2013**, *224*, 2225−2248.
(28) Veerapaneni, S.; Wiesner, M. Hydrodynamics of fractal aggregates with radially varying permeability. *J. Colloid Interface Sci.* **1996**, *177*, 45−57.
(29) Johnson, C. P.; Li, X.; Logan, B. E. Settling velocities of fractal aggregates. *Environ. Sci. Technol.* **1996**, *30*, 1911−1918.
(30) Bradford, S.; Torkzaban, S.; Walker, S. Coupling of physical and chemical mechanisms of colloid straining in saturated porous media. *Water Res.* **2007**, *41*, 3012−3024.
(31) Bradford, S.; Simunek, J.; Bettahar, M.; van Genuchten, M.; Yates, S. Modeling colloid attachment, straining, and exclusion in saturated porous media. *Environ. Sci. Technol.* **2003**, *37*, 2242−2250.
(32) Chowdhury, I.; Walker, S.; Mylon, S. Aggregate morphology of nano-TiO 2: role of primary particle size, solution chemistry, and organic matter. *Environ. Sci.: Process. Impacts* **2013**, *15*, 275−282.
(33) Liu, Q.; Lazouskaya, V.; He, Q.; Jin, Y. Effect of Particle Shape on Colloid Retention and Release in Saturated Porous Media. *J. Environ. Qual.* **2010**, *39*, 500−508.
(34) Salerno, M. B.; Flamm, M.; Logan, B. E.; Velegol, D. Transport of Rodlike Colloids through Packed Beds. *Environ. Sci. Technol.* **2006**, *40*, 6336−6340.
(35) Seymour, M.; Chen, G.; Su, C.; Li, Y. Transport and Retention of Colloids in Porous Media: Does Shape Really Matter? *Environ. Sci. Technol.* **2013**, *47*, 8391−8398.
(36) Xu, S.; Liao, Q.; Saiers, J. Straining of Nonshperical Colloids in Saturated Porous Media. *Environ. Sci. Technol.* **2008**, *42*, 771−778.
(37) Weiss, T. H.; Mills, A. L.; Hornberger, G. M.; Herman, J. S. Effect of Bacterial Cell Shape on Transport of Bacteria in Porous Media. *Environ. Sci. Technol.* **1995**, *29*, 1737−1740.
(38) Zhou, D.; Keller, A. A. Role of morphology in the aggregation kinetics of ZnO nanoparticles. *Water Res.* **2010**, *44*, 2948−2956.
(39) Oles, V. Shear-Induced Aggregation and Breakup of Polysterene Latex Particles. *J. Colloid Interface Sci.* **1992**, *154*, 351−358.
(40) Wei, D.; Wu, H.; Xia, Z.; Xie, D.; Zhong, L.; Morbidelli, M. Monitoring coalescence behavior of soft colloidal particles in water by small-angle light scattering. *Colloid Polym. Sci.* **2012**, *290*, 1033−1040.
(41) Zaccone, A.; Gentili, D.; Wu, H.; Morbidelli, M. Shear-induced reaction-limited aggregation kinetics of Brownian particles at arbitrary concentrations. *J. Chem. Phys.* **2010**, *132*, 134903.
(42) Gregory, J. Interaction of unequal double layers at constant charge. *J. Colloid Interface Sci.* **1975**, *51*, 44−51.
(43) Gregory, J. Approximate expressions for retarded van der Waals interaction. *J. Colloid Interface Sci.* **1981**, *83*, 138−145.
(44) Elimelech, M.; Gregory, J.; Jia, X. *Particle Deposition and Aggregation: Measurement, Modelling and Simulation*; Butterworth-Heinemann, 2013.
(45) Torkzaban, S.; Bradford, S. A. Critical role of surface roughness on colloid retention and release in porous media. *Water Res.* **2016**, *88*, 274−284.
(46) Husband, J.; Adams, J. Shear-induced aggregation of carboxylated polymer latices. *Colloid Polym. Sci.* **1992**, *270*, 1194−1200.
(47) Schindelin, J.; Arganda-Carreras, I.; Frise, E.; et al. Fiji: an open-source platform for biological-image analysis. *Nat. Methods* **2012**, *9*, 676−682.
(48) Doube, M.; Klosowski, M.; Arganda-Carreras, I.; Cordelieres, F.; Dougherty, R.; Jackson, J.; Schmid, B.; Hutchinson, J.; Shefelbine, S. BoneJ: free and extensible bone image analysis in ImageJ. *Bone* **2010**, *47*, 1076−1079.

https://dx.doi.org/10.1021/acs.est.9b05744
Environ. Sci. Technol. 2020, 54, 5813−5821

(49) Lee, C.; Kramer, T. Prediction of three-dimensional fractal dimensions using the two-dimensional properties of fractal aggregates. *Adv. Colloid Interface Sci.* **2004**, *112*, 49−57.
(50) Soos, M.; Moussa, A.; Ehrl, L.; Sefcik, J.; Wu, H.; Morbidelli, M. Effect of shear rate on aggregate size and morphology investigated under turbulent conditions in stirred tank. *J. Colloid Interface Sci.* **2008**, *319*, 577−589.
(51) Bradford, S. A.; Simunek, J.; Bettahar, M.; Van Genuchten, M. T.; Yates, S. R. Significance of straining in colloid deposition: Evidence and implications. *Water Resour. Res.* **2006**, *42*, W12S15.
(52) Veerapaneni, S.; Wiesner, M. Deposit morphology and head loss development in porous media. *Environ. Sci. Technol.* **1997**, *31*, 2738−2744.

https://dx.doi.org/10.1021/acs.est.9b05744
Environ. Sci. Technol. 2020, 54, 5813−5821